Core–Shell Nanoparticle Interface and Wetting Properties

*Joakim Engström, Calvin J. Brett, Volker Körstgens, Peter Müller-Buschbaum,
Wiebke Ohm, Eva Malmström,* and Stephan V. Roth**

Latex colloids are among the most promising materials for broad thin film applications due to their facile surface functionalization. Yet, the effect of these colloids on chemical film and wetting properties cannot be easily evaluated. At the nanoscale, core–shell particles can deform and coalesce during thermal annealing, yielding fine-tuned physical properties. Two different core–shell systems (soft and rigid) with identical shells but with chemically different core polymers and core sizes are investigated. The core–shell nanoparticles (NPs) are probed during thermal annealing in order to investigate their behavior as a function of nanostructure size and rigidity. X-ray scattering allows to follow the re-arrangement of the NPs and the structural evolution in situ during annealing. Evaluation by real-space imaging techniques reveals a disappearance of the structural integrity and a loss of NP boundaries. The possibility to fine-tune the wettability by tuning the core–shell NPs morphology in thin films provides a facile template methodology for repellent surfaces.

1. Introduction

Thin film applications of latex colloids[1,2] range from structural colors[3] to advanced functional templates.[4] Recently,

Dr. J. Engström, C. J. Brett, Prof. E. Malmström, Prof. S. V. Roth
KTH Royal Institute of Technology
Department of Fibre and Polymer Technology
Division of Coating Technology
Wallenberg Wood Science Center
Teknikringen 56–58, SE-10044 Stockholm, Sweden
E-mail: mavem@kth.se; svroth@kth.se

C. J. Brett
Department of Mechanics
KTH Royal Institute of Technology
Teknikringen 8, SE-10044 Stockholm, Sweden

C. J. Brett, Dr. W. Ohm, Prof. S. V. Roth
Deutsches Elektronen-Synchrotron (DESY)
Notkestrasse 85, 22603 Hamburg, Germany
E-mail: stephan.roth@desy.de

Dr. V. Körstgens, Prof. P. Müller-Buschbaum
Technische Universität München
Physik-Department
Lehrstuhl für Funktionelle Materialien
James-Franck-Str. 1, 85748 Garching, Germany

Prof. P. Müller-Buschbaum
Heinz Maier-Leibnitz Zentrum (MLZ)
Technische Universität München
Lichtenbergstr. 1, 85748 Garching, Germany

this approach has been extended to non-iridescent structural colors with broad spectral and angular range for use in flexible displays.[5] Fundamentally, colloids can be considered as "large-scale" atoms with adjustable size which can be assembled similar to atoms in a crystal.[4,6–8] Colloidal latex film formation is a complex process involving different phases of drying, removal of water, particle re-arrangement, interparticle chain-diffusion, and eventually coalescence.[2,7,9,10] On the nanoscale, core–shell particles can deform and coalesce during thermal annealing yielding fine-tuned physical properties.[2] The quest for improving the colloidal stability of a latex and its film-forming properties has led to exploring covalently attached surfactants; these are either reactive surfmers[11,12] or concepts of surfactant-free emulsion polymerization techniques.[13] Among the latter, two techniques have proven to be effective, namely free radical polymerization, and controlled radical polymerization (RDRP).[14,15] One of the earliest studies on the synthesis of latex particles via emulsion polymerization resulted in particles forming a coalesced film already at ambient temperatures. Since then, latexes of poly(vinyl acetate) have been extensively utilized in commercial wood adhesives.[16] The main advantage of emulsion polymerization is the production of hydrophobic polymers of high molecular weight in water dispersions at high dry contents but low viscosities.[17] Emulsion polymerization also offers many possibilities to vary the constituents depending on the targeted application demands in adhesives, painting, textiles, and paper industries.[18] The major components used for latex synthesis are: water, initiator, emulsifier/surfactant, and hydrophobic monomer/s.[9] The choice of components affects the film properties due to the glass transition temperature T_g of the core polymer and possible migration of non-covalent surfactants.[11] Tailoring surface contact angle (CA) based on micro- and nanostructuring as well as by chemical modifications allows for large CA variations.[19,20] However, it is yet still a challenge to fine-tune a CA by minimal material usage.[21] Hence, the aim of this manuscript is to show the fine-tuning by low surface coverage induced CA changes.

One of the recent developments to further improve latexes and to utilize block copolymers in the latex production is polymerization-induced self-assembly (PISA).[14,22] In such an approach, a hydrophilic polymer (commonly a macro reversible addition-fragmentation chain-transfer (RAFT) agent[23,24]) is chain extended in situ with hydrophobic monomers. When the hydrophobic part becomes long enough, nucleation of nanoparticles (NPs) occurs. Thereafter, subsequent diffusion of

monomers into the core of the particles sustain the controlled polymerization in the core, thus resulting in high monomer conversion and a narrow molecular weight distribution.[15] The result is core–shell NPs, dispersed in water[25] as a consequence of the amphiphilic nature of the block copolymer. Conceptually, this approach paves the way for a versatile pathway to introduce functionality in hydrophilic, stabilizing corona. The surface functionality can be tailored so as to govern strong interactions, as previously exemplified by a cationic or xyloglucan-based corona which interacts strongly with anionic surfaces, such as charged nanocellulose and silica.[26,27] These newly established core–shell surface-interacting NPs, made of block copolymers, and their coatings require characterization and fundamental understanding at the nanoscale, due to their larger complexity compared to conventional latexes.[26] Knowing the complex nanostructures, the NP's thin film formation behavior and the effect of annealing at different temperatures raise fundamental questions such as: how do the NP core–shell boundaries alter? How do the different polymer glass transition temperatures (T_g) affect the structural evolution in a thin coating? This has not been studied for polymeric cationic core–shell NPs. In order to do so, thin films with individual NPs must be fabricated. Among other thin film methods available as dip-coating[28–31] and spin-coating,[32,33] airbrush spray deposition[34,35] is a widely applied, rapid and easily scalable technique. Spray deposition is a very versatile method for nanostructuring due to tuneable homo- or heterogeneous droplets or deposition on 3D shapes as in car manufacturing.[36,37] Nowadays, spray deposition is also well established for thin films in combination with in situ X-ray scattering techniques to study the nanoscale self-assembly of particles.[35,38–40] Different spray-coating devices have been applied in both industry and academia for a long time depositing conventional colloids, however more recently focused on more advanced colloidal systems and NPs including gold,[41] silica,[42] Cu_2FeSnS_4,[43] polymeric,[44] and titanium dioxide.[45] Previous studies investigated how both drying and annealing of thin films of NPs can be analysed in situ and result in various functional high-end applications[40,46] as well as following the PISA process itself[22] using both *transmission* small-angle X-ray scattering techniques (SAXS) and surface sensitive grazing incidence SAXS (GISAXS). [47]

Scattering investigations allow for observation of particle chain interdiffusion and coalescence, i.e., disruption of boundaries for the once spherical colloids, known to be affected by the type of stabilizing components.[48–51] Previous studies on thermal stability of anionic polystyrene NPs reported that the particles soften at the boundaries, largely affecting the nanostructure while macroscopic features, such as refractive index, remain constant.[52] Together with imaging tools such as transmission electron microscopy (TEM),[53] field-emission scanning electron microscopy (FE-SEM),[54,55] and atomic force microscopy (AFM)[47] it is possible to follow the drying and annealing of latex/NPs and to investigate the effect of the surface/film properties. This allows insight in the driving forces for film formation, commonly discussed to be driven by the air-polymer surface tension (during the dry sintering) or capillary forces in the more wet state.[26,56–58] Knowing the complexity of drying mechanisms and how to study this phenomenon, it is interesting to start investigating the spherical boundaries of the NPs in thin film coatings, which in turn can give understanding of the macroscale film formation at denser layers.

(Hydrophobic) core–(hydrophilic) shell NPs from RAFT-mediated PISA using emulsion polymerization are synthesized and their structural wetting behavior is studied. Spray-deposited thin films are annealed and investigated in situ using GISAXS and correlated to real-space AFM and FE-SEM measurements. The observed NP structural evolution at the nanoscale combined with contact angle measurements (CAM) is used to correlate the effect of nanostructures on the wettability. The annealing from room temperature up to 140 °C is followed, comparing two types of core polymers, poly(methyl methacrylate) (PMMA) ($T_g \approx 126$ °C) and poly(butyl methacrylate) (PBMA) ($T_g \approx 36$ °C) each in small and large NPs. The structural evolution of the core–shell NPs, as analysed and presented in this study, allows to tailor NP morphologies and resulting wettability for high-end applications, such as nanostructured sensors.

2. Results and Discussion

Colloidal NPs having a hydrophilic shell based on *N,N*-dimethylaminoethyl methacrylate (DMAEMA) and a hydrophobic core composed of PMMA or PBMA were synthesized by RAFT-mediated surfactant-free emulsion polymerization. In the first step, DMAEMA is polymerized (PDMAEMA) and then subsequently chain extended with either methyl methacrylate (MMA) or butyl methacrylate (BMA). Once the hydrophobic block is long enough, the NPs starts to form by self-assembly of the diblock copolymers. The resulting core–shell NPs, **Table 1**, are stabilized by their hydrophilic shell that is why no low-molecular weight surfactant is needed. The synthesized core–shell NPs are spray-deposited onto silicon substrates to form a homogeneous sub-monolayer thin coating. These surfaces are

Table 1. Characteristics of the core–shell NPs. The notation of the core–shell NPs is given by their core polymer type (PMMA or PBMA) and the index S and L relates to the hydrodynamic sizes small and large, respectively.

Name	DP[a]	Charge density [µeq g⁻¹][b]	Tg [°C][c]	PDI[d]	DH [nm][d]	ζ [mV][e]
PMMA$_S$	176	1000 ± 150	125 ± 3	0.14 ± 0.03	37 ± 1	$+41 \pm 2$
PMMA$_L$	1410	114 ± 9	126 ± 3	0.04 ± 0.02	96 ± 1	$+40 \pm 2$
PBMA$_S$	176	430 ± 10	35 ± 1	0.10 ± 0.02	32 ± 1	$+43 \pm 2$
PBMA$_L$	1410	87 ± 1	37 ± 1	0.03 ± 0.02	82 ± 1	$+40 \pm 2$

[a]Targeted theoretical degree of polymerization for the hydrophobic core polymer PMMA or PBMA, conversion analyzed by gravimetric analysis[26]; [b]Charge density measured by PET[26]; [c]Glass transition temperature T_g as measured by DSC; [d]Measured by DLS in MilliQ-water; [e]Measured by DLS in 1×10^{-3} M KCl at 0.1 g L⁻¹.[26]
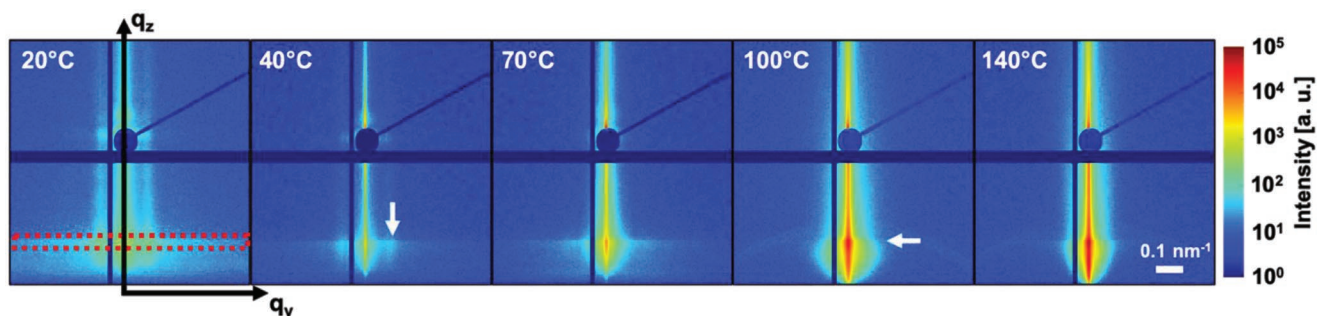
Figure 1. 2D GISAXS data of the sprayed PMMA$_L$ thin film at different annealing temperatures (from left to right; 20, 40, 70, 100, and 140 °C). The Yoneda region for PMMA is marked with the red dashed box. With increasing temperature, the side peaks at $T = 20$ °C, indicating a well-ordered structure (vertical white arrow), gradually decrease and the Yoneda peak (indicated by the horizontal white arrow) increases, indicating a roughening of the nanostructure.

analysed by GISAXS to follow the film formation and the structural evolution during annealing. Subsequently, the thin films are studied ex situ using AFM, FE-SEM, and CAM to correlate the nanoscale changes to macroscopic physical properties.

2.1. Structure Evolution

The NPs structural evolution is studied on spray-deposited silicon substrates in situ during thermal annealing. The obtained GISAXS scattering pattern is analysed at the Yoneda peak for PMMA ($\alpha_c = 0.116°$) and PBMA ($\alpha_c = 0.112°$), see **Figure 1** and Figure S1 in the Supporting Information. Data reduction is performed by integration along q_y (red dashed box), shown in **Figure 2**, for all latexes at five different temperatures (20, 40, 70, 100, and 140 °C). This allows the comparison to previously published work by Herzog et al. on thermally annealed polystyrene NP thin films.[52]

The GISAXS data in Figure 1 and the corresponding cuts in Figure 2 show that the thin films undergo structural evolution and change during annealing. However, the GISAXS pattern do not change drastically until temperatures above 70 °C, despite
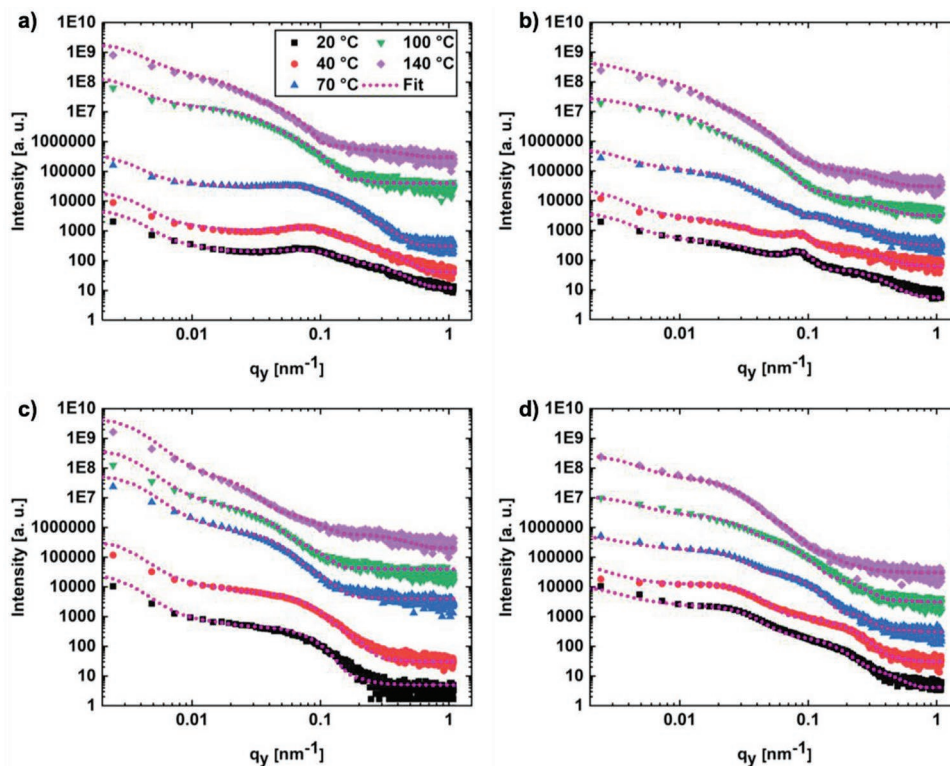

Figure 2. 1D intensity distribution along q_y-axis integrated at the polymers corresponding Yoneda region. All samples are stepwise annealed: 20 °C (black), 40 °C (red), 70 °C (blue), 100 °C (green), 140 °C (purple), and the cumulative fit (magenta). a) PMMA$_S$, b) PMMA$_L$, c) PBMA$_S$, and d) PBMA$_L$. The shoulders originate from NP sizes, while the very distinct peaks at low temperature seen in a,b) originate from the structure factor of well-ordered structures. In d) two shoulders can be observed which are due to two distinct sizes which are not overlapping as in other cases. All data is shifted vertically for better visualization.

that the NPs have different measured T_g's for the core polymers; $T_{g,\,PMMA} \approx 126\,°C$, and $T_{g,PBMA} \approx 36\,°C$.[26] Both NPs with either PMMA or PBMA in the core show a distinct change at 70 °C, which for PMMA is below its measured T_g and for PBMA above. These results indicate that some structural evolution occurs independent of T_g of the core. One plausible explanation might be that for example PMMA commonly show broader and different apparent T_g's depending on particle size, tacticity, and interactions at the interfaces.[59,60] Therefore, we speculate that the observed behavior with increased temperature could be attributed to the increased core polymer chain mobility starting at 70 °C for both core polymers. Adding the partial softening of the NPs as previously shown by Herzog et al.[52] and decreased charge repulsion due to the loss of bound water in the otherwise cationic polymeric shell could explain these rapid morphological changes. Keddie et al. studied the drying of similar but anionic latexes (from PISA) with SANS and could show varying morphologies all the way to 100% dry content, resulting in no further change upon annealing for 24 h at 100 °C. Hence, the most crucial step is the annealing before the latex is fully dry, when there is still some mobility of all chains in the block copolymers. No distinct structural changes in the GISAXS pattern above 70 °C were observed (Figures 1 and 2).

The GISAXS data for the NP-coated silicon substrates in Figure 2 are fitted using a spherical form factor on a paracrystal plane, adopted from Schaffer et al.[61] Details of the fitting can be found in the Supporting Information (SI) and are elaborated in Figure S2 in the Supporting Information on the example of PMMA_L. The fitting is based on the assumption that these NPs

are spherical and did not deform upon spray deposition. For all the four different NP types, it is possible to extract two distinct spherical domains with corresponding distances to each other (d_1 and d_2): a smaller domain size which directly correlates well with the individual NP size as measured in AFM and a larger domain size which can be attributed to the aggregated or coalesced particles on the surface, r_2 and r_1, respectively. The summary of all interdomain distances and domain sizes with increasing temperature resulting from the annealing (room temperature up to 140 °C) is shown in **Figure 3** as a result from the fit of the line cuts in Figure 2. The smallest PMMA_S NPs do not change in size or distance until a temperature of 70 °C is reached, resulting in an increase both in the horizontal size of the individual particles as well as their corresponding distances, see Figure 3a. The larger domain size increases faster than the smaller, indicating softening of the NPs and possibly coalescence. The PMMA_L NPs behave differently than the PMMA_S. The domain size (= $2 \times r_2$) alters slightly before 70 °C; the final smallest domain distance does not alter during the whole annealing sequence. The larger domains increase in size, indicating that the particles re-arrange and coalesce to finally form a smooth thin film. The PBMA NPs undergo a similar transformation. Due to their lower T_g, they are already deformed after drying at room temperature after the spray deposition. Therefore, they show softening, and clusters due to coalescence already at room temperature, similar to the observations using AFM-imaging of NP-coated cellulose surfaces.[26] The PBMA_S NPs follow a similar trend as the PMMA_S (Figure 3c). The larger NPs, PBMA_L (Figure 3d) show no significant difference
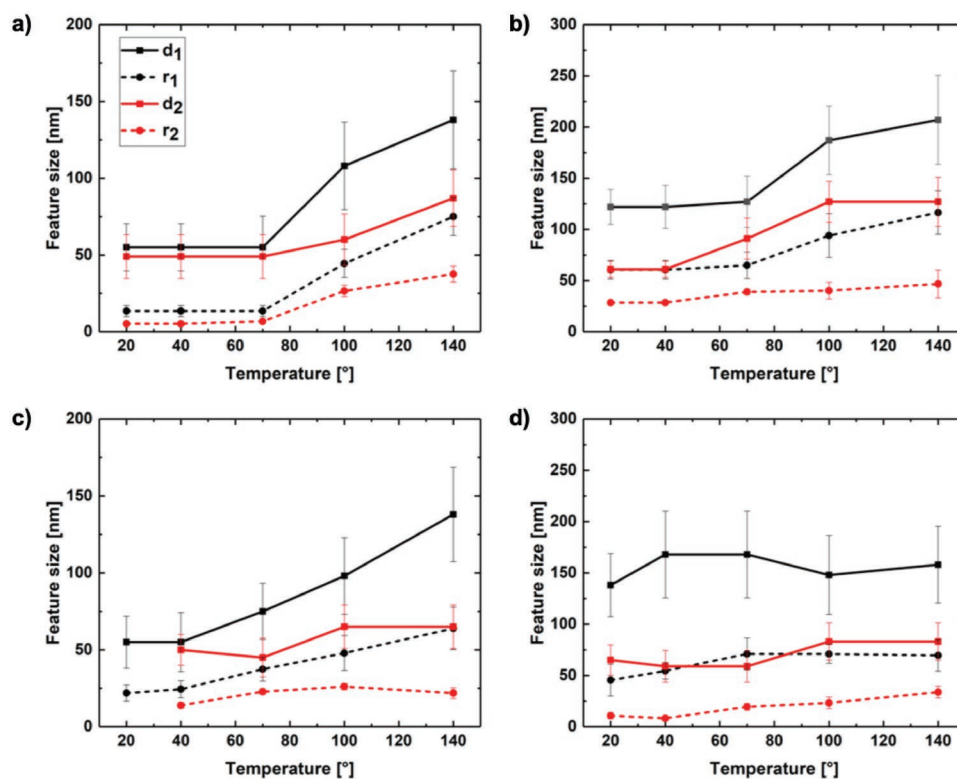
Figure 3. Feature size evolution during thermal annealing. The feature sizes correlate to two radius $r_{1,2}$ and distances $d_{1,2}$ to each other of the NPs. The index is connecting the two distinct sizes which were found. Shown are a) PMMA_S, b) PMMA_L, c) PBMA_S, and d) PBMA_L.

ADVANCED
SCIENCE NEWS
www.advancedsciencenews.com

ADVANCED
FUNCTIONAL
MATERIALS
www.afm-journal.de

in the size and distance between domains for the whole temperature range. As they form clusters at room temperature, the changes above 70 °C for PBMA$_S$ are not that pronounced. One could speculate that the increased temperature up to 70 °C allows the polymer chains to re-organize and only slight deformation is observed.[26]

The large PBMA$_L$ NPs are instead almost unaffected by thermal annealing, which can be attributed to the aggregation/cluster formation at room temperature and scarcer spreading of clusters. Comparing the two core polymers, it seems that the domain size changes less distinctly for the PBMA latexes and more distinctively above 70 °C for the PMMA latexes, possibly governed by the stabilizing corona of PDMAEMA being repulsive. Comparing the large and small PMMA/PBMA NPs, the main difference is the length of the core polymer (i.e., degree of polymerization (DP) of PMMA/PBMA) set during the PISA formation of the NPs. Targeting the larger size of the core–shell NP is given by a larger molecular weight of the core polymer. In this study, the DP target values are 176 for small and 1410 for large NP. This gives a very different final relative wt% of the two different core–shell polymers, since all NPs have the same shell polymer (PDMAEMA, DP = 25).[26] Therefore, the four NP types come in four different ratios of hydrophilic cationic polymer in the shell to the hydrophobic polymer in the core. The shell polymer is very hydrophilic and causes repulsion in wet state. The stiffer the core, the longer the NPs maintain/retain their spherical integrity and in addition their hydrophilic/repulsive character if maintained wet. In conjunction with the increasing ratio of hydrophobic polymer to hydrophilic shell with increasing size (25:176 compared to 25:1410 for the small and large NPs, respectively), this leads to less repulsive forces to hinder interparticle interactions and chain diffusion. This could explain why the behavior is so different for PBMA$_S$ and PBMA$_L$ upon annealing. This relates back to and is strengthened by the large change in structural evolution for the samples above 70 °C, where we speculate an increased evaporation of water.

2.2. Nanoscale Appearance

In order to correlate the results obtained from Figures 2 and 3, further analysis using high-resolution real-space imaging was applied on the NP-coated silicon surfaces at room temperature, see **Figure 4**. The topographical AFM images show that the NPs with PMMA in the core appear spherical at room temperature, see Figure 4a,b. On the contrary, the NPs with PBMA in the core seem to deform and to form clusters already at room

temperature (Figure 4c,d). The cluster formation due to coalescence is well pronounced for the larger PBMA$_L$ NPs compared to the smaller sized PBMA$_S$. This indicates that the cluster formation is facilitated. This behavior can also explain the initial larger domain sizes r_1 observed in the GISAXS measurements (Figure 3d). The smaller PBMA$_S$ does appear as more spherical particles compared with the large pre-aggregated PBMA$_L$.

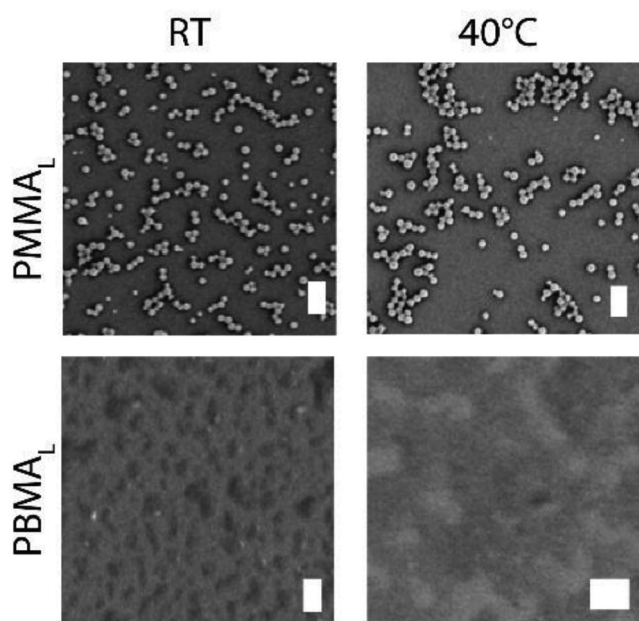The distinct difference between the PMMA- and PBMA-NPs is directly related to the different T_g's of the core polymers and is shown with height measurements in the Supporting Information. The height and lateral dimensions are extracted from Figure 4 (shown in Figures S3–S6 are summarized in Table S1, Supporting Information). The lateral dimensions correlate well with the hydrodynamic diameter as well as with the GISAXS results at room temperature. The hydrodynamic diameter of the PMMA NPs (Table 1), correlates well with the measured height and width in AFM (Table S1, Supporting Information), as shown before on cellulose and silica surfaces.[26,27] In contrast the low T_g latexes (PBMA) show large deviations in the height compared to the hydrodynamic size, thus indicating the flattening and aggregation already at room temperature. The AFM images also show that the PBMA$_L$ NPs clearly do not form a defined colloidal film after drying at room temperatures and do not alter in size with higher temperatures; though they form a smoother film, corroborating the GISAXS results in Figures 2 and 3. Larger area topographic maps can also be found in Figure S3 in the Supporting Information.

To further evaluate the core–shell NPs on silicon surfaces, FE-SEM was conducted to study the nanoscale surface topography, see **Figure 5**. The combination of AFM and FE-SEM allows the distinction of spherical clusters and coalesced particles with distinct disrupted particle boundaries. The difference between the size is less distinct from FE-SEM, see Figure S6 in the Supporting Information. Comparing the largest NPs PMMA$_L$ and PBMA$_L$ in Figure 5, there is a clear difference between the NPs at room temperature. PMMA$_L$ shows maintained spherical particle morphology. PBMA$_L$ indicates clusters and nanostructures with low contrast. This goes along with the results in Figure 4: There is no sign of maintained particle boundaries.

Additionally, FE-SEM was performed on samples after 1 h at 40 °C for annealing of the thin films. The FE-SEM corroborates the GISAXS data in Figure 3, showing that there is none or little structural evolution of PMMA$_L$ together with the rather maintained size of the domains for PBMA$_L$ up to 40 °C. Thermal annealing alters the particle appearance from spherical to flat and more spread on the surface as the temperature rises.
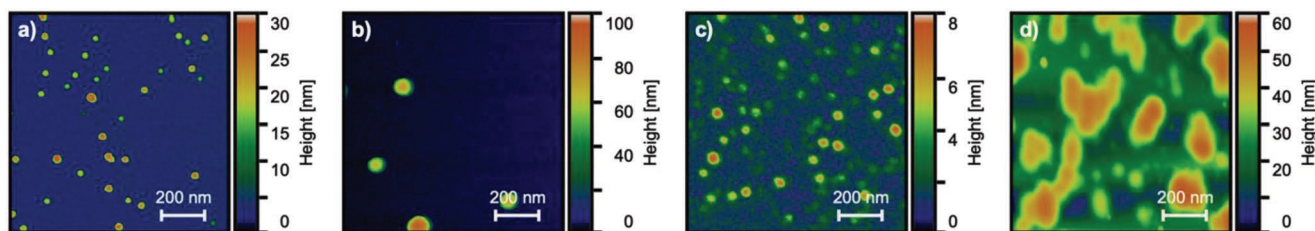
Figure 4. Topographic AFM images of the PISA-latexes on silicon substrates. a) PMMA$_S$, b) PMMA$_L$ c) PBMA$_S$, and d) PBMA$_L$. Scale bar is adjusted to enhance the height features.

ADVANCED
SCIENCE NEWS
www.advancedsciencenews.com

ADVANCED
FUNCTIONAL
**MATERIALS**
www.afm-journal.de

Figure 5. SEM analysis of silicon substrates spray coated with NPs PMMA$_L$ and PBMA$_L$ before and after annealing at 40 °C. Scale bar is 200 nm. The boundaries for the PMMA$_L$ are clearly maintained at T = 40 °C, while a roughened surface is visible for PBMA$_L$ without clear NP boundaries, corresponding to the GISAXS data in Figure 3.

As visualized by AFM, the surface coverage is low for any of the NPs layers. An estimated number of NPs per µm² can be seen in Table S2 in the Supporting Information. The estimate is based experimentally on local AFM images as well as theoretically calculated form the known deposition. Both approaches show a similar trend. The difference in numbers can be readily explained with the so-called coffee ring effect which occurs when particle-loaded suspensions are deposited and the droplet dries. The droplets will deposit different amount of particles depending on the position within the deposited droplet. Most particles will be found on the edge of the former droplet, and a coffee ring appears. This phenomenon has been previously extensively studied and is well known in spray-deposited thin films.[62] This desired and targeted low number of NPs per area unit means that the analysis is indeed for sub-monolayers and

the resulting effect on surface wetting will be more affected by the chemical nature of the NP and not secondary roughness as for multilayers.[19]

2.3. Wettability

To relate the NP structural evolution from GISAXS and high-resolution real-space imaging to wetting properties, being an important application for functional coatings, CAM were performed for spray-coated samples before and after thermal annealing at 40 and 140 °C, respectively. The observed CAs of the coatings resulted in angles above 60° for all samples, despite the incomplete surface coverage, see **Figure 6**. A reference cleaned silicon surface was annealed following the same procedures showing full spreading of a water droplet after drying at room temperature and a water CA of $(61 \pm 1)°$ for treatment at 140 °C. The transition seen at 70 °C for all NPs in GISAXS, Figures 2 and 3, can be observed also by an increasing value of CA for surfaces coated with PMMA and PBMA core–shell NPs, as the CA changes between 40 and 140 °C. Seemingly all NP-coatings need annealing up to or above 70 °C so that the surface properties are dominated by the core polymers, further indicating the importance of the particle–particle interface and core–shell properties of these specific NPs. The core–shell properties especially present in PBMA NPs lead to hydrophobic thin films already at room temperature. The literature value for water CA on PMMA is around 60°, but the hydrophobicity has been shown to increase by alignment of polymer chains or an increase in surface roughness.[26,63] As the film forms only sub-monolayer, the roughness dependency can be neglected. Therefore, we speculate that the polymer chains could align within the thin film during the annealing process as the NPs coalesce, thus yielding higher CA. The low NPs coverage and the resulting small changes in CA's allow very precise fine-tuning of wettability. This is of great importance for applications where the surface energy yields a change by a few degrees in CA retaining other physical properties such as light transmission and accessability of the surface. This is highly beneficial for chemical sensor applications.[20] Modifications of the CA by less than 5° were shown to directly result in higher conductive conjugated polymer-based contacts in organic solar cells.[64] For perovskite solar cells, it was reported that small
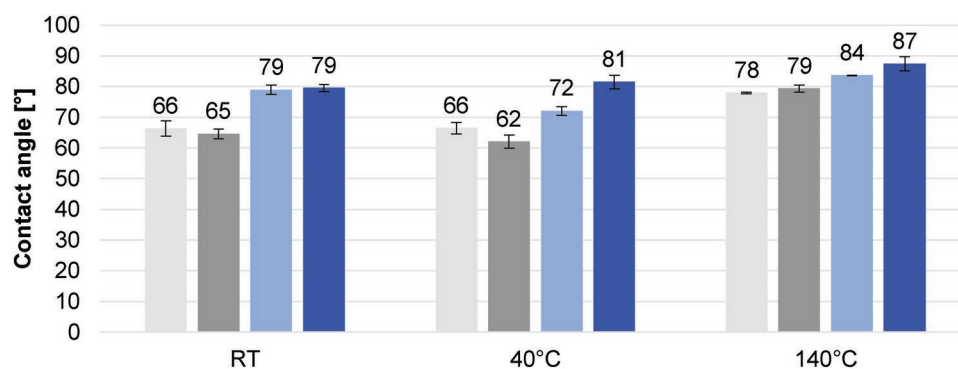
Figure 6. CAM of water droplets on silicon surfaces coated with the NPs and treated for 1 h at 40 and 140 °C for annealing. Light grey: PMMA$_S$, grey: PMMA$_L$, light blue: PBMA$_S$, and blue: PBMA$_L$. The numbers on top of the bars indicate the averaged CA (averaged over three droplets).

variations in CA yield to macroscopic differences in film formation which directly affects the efficiency.[65] Menzies and Jones correlated slight changes in CAs to immediate changes in cell–cell interactions in tissue engineering.[21]

3. Conclusion

In order to fully understand and tailor functional coatings of NPs with core–shell structures, it is crucial to elucidate their nanostructure-wetting relationship, thus being able to fine-tune the CA. A spray-deposited sub-monolayer of two different NP systems (core of either PMMA and PBMA with stabilizing shell of a cationic polymer) is studied to follow the morphological changes that induce differences in water wetting behavior. The NPs boundaries are affected by its core–shell nanostructure and their size. The disappearance of the NPs integrity is investigated during thermal annealing (RT up to 140 °C) by a combination of GISAXS, FE-SEM, AFM, and CAM, allowing to characterize the particle morphology and to follow the structural evolution. NPs with PMMA in the core show that annealing above T_g is required for film formation and to increase the hydrophobicity of the surface. The PBMA NPs show initial film and cluster formation already at room temperature. AFM imaging reveals that PBMA NPs show flattened domains at room temperature, with distinct particle boundaries maintained, despite a hydrophobic surface. The NP domain morphology alters for all films up to 140 °C, where all NP-coated surfaces also reach highest hydrophobicity. The small changes in CA indeed confirm our ability to fine-tune the CA. The functionality and complexity of these NPs relates back to the fact that these are block copolymers, with the stabilizing shell being a hydrophilic polymer and a hydrophobic core polymer, thus able to re-organize and possibly self-assemble upon increasing temperatures. Understanding how functional core–shell NPs maintain or alter their particle morphology and boundaries in situ during annealing allows controlling the morphology at both nano- and macroscale. Our results show how the alteration—induced by adjustable external temperature—of the nanostructure of the individual core–shell colloids and their interface between them crucially affects the wetting properties of even scarce colloidal films. This fundamental understanding will allow for creating controllable functional hybrid colloidal arrays making use of adjustable chemical surface properties in facile way.

4. Experimental Section

Materials: DMAEMA (Aldrich, 98%), MMA (Acros, 99%), BMA, Sigma–Aldrich, 99%), 2,2′-azobis(2-methylpropionamidine) dihydrochloride (AIBA, Aldrich, 97%), 1,3,5-trioxane (Aldrich, ≥99%), sodium chloride (VWR), were used as received. The RAFT agent, 4-cyano-4-thiothiopropylsulfanyl pentanoic acid, was prepared according to literature procedures by reacting 4,4-azobis(4-cyanopentanoic acid) with bis(propylsulfanylthiocarbonyl) disulfide.[24,66,67] MilliQ-water (18.2 MΩ cm^{-1}) was used, unless otherwise noted.

Substrates: Pre-cut, polished silicon wafers (20 × 20) mm^2 (Si-Mat, Germany) were cleaned by sonicating them in acetone for 15 min. The wafers were subsequently rinsed by acetone, 2-propanol, and ethanol (VWR Chemicals) and further cleaned in 315 mL piranha solution (87.5 mL hydrogen peroxide 30%, 190 mL sulfuric acid 96%, 37.5 mL

MilliQ-water) for 15 min at 80 °C, followed by a 2 min rinsing with MilliQ-water. The cleaned substrates were then kept in MilliQ-water until use and dried just minutes prior the spray deposition by applying a flow of nitrogen.[35,39]

Latex Fabrication: Core–shell NPs of PMMA or PBMA in the core (latexes) were obtained using a pre-formed PDMAEMA-based macroRAFT synthesized in water according to a previously reported procedure.[26,27] The latex characteristics are presented in Table 1. In a typical experiment to produce PMMA NPs, the macroRAFT agent (0.150 g, 38 µmol for DP = 25) was added to a 25 mL round bottom flask equipped with a magnetic stirring bar followed by addition of deionized water (13.2 mL). The monomer, MMA (2.56 g, 25.6 mmol) was added. An aqueous solution of the initiator AIBA (3.4 g L^{-1}) was added to the reaction mixture (1.19 mg, 4.4 µmol in 1:8.25 molar ratio to the macroRAFT). The flask was placed in a water/ice bath and the reaction mixture was degassed with argon for 30 min and thereafter immersed into an oil bath which was pre-heated to 70 °C, reacting for 2 h. The conversion of monomer was monitored by gravimetric analysis of the dry content by withdrawing samples during the reaction. The NPs were analysed in the wet state by polyelectrolyte titration (PET) and dynamic light scattering (DLS), and in the dry state, using differential scanning calorimetry (DSC).

Instrumentation and Methods–Polyelectrolyte Titration: The inherent charge density was measured for all NPs using a 716 DMS Titrino (Metrohm, Switzerland) with potassium poly(vinyl sulfate) (KPVS) as the titrant and ortho-toluidine blue as the indicator. The change in color was recorded with a Fotoelektrischer Messkopf 2000 (BASF) and the amount of KPVS needed to titrate to equilibrium was calculated according to the method described by Horn.[68]

Dynamic Light Scattering: The hydrodynamic diameter (D_H), polydispersity index (PDI), and electrophoretic mobility (zeta potential, ζ) of the NPs were determined with a Malvern Zetasizer NanoZS at 25 °C. The values for the zeta potential were added in Table 1, no significant changes were observed. For the particle size measurements, two concentrations were used (3 and 0.1 g L^{-1}), and the particles were diluted in pure MilliQ-water.

Differential Scanning Calorimetry: NPs were dried prior to analysis performed with a Mettler Toledo DSC, using a heating and cooling rate of 10 °C min^{-1} under a nitrogen atmosphere. The heating and cooling method used was: heating from −60 to 150 °C, equilibrium for 5 min and then cooling from 150 to −60 °C, equilibrium for 5 min and a second heating from −60 to 150 °C. Data from second heating were used to calculate the glass transition temperature for all samples.

Spray Deposition: The NP dispersions were diluted with MilliQ-water to 0.1 vol% for spray deposition. Latex dispersions were left in sonication bath for 10 min prior to spraying. Spray deposition was performed with an airbrush device (D55500, Spray Systems, Germany) using single spray pulses of 50 ms and 1 mL min^{-1} flow rate.[35] The nozzle-to-substrate distance was 200 mm in the very dilute spray regime where the droplet size is very homogeneous and about 4.5 µm in diameter (as stated by manufacturer).[38,69]

Grazing Incidence Small-Angle X-Ray Scattering: GISAXS measurements were performed at the MiNaXs/P03 beamline at PETRA III at the Deutsches Elektronen-Synchrotron (DESY), Germany.[70] The X-ray wavelength and the beam size were 0.1088 nm and (28 × 24) µm^2 (horizontal × vertical), respectively. The Pilatus 1M detector (Dectris Ltd., Switzerland) with a pixel size of (172 × 172) µm^2 was employed to collect 2D GISAXS patterns. The sample-to-detector distance was (4720 ± 1) mm. The incident angle α_i was set to 0.42°, which is above the critical angles for total reflection of the polymer and the silicon substrate and allows for full penetration into the applied thin film. The integration time for the all measurements was set to 100 ms. To avoid beam damage during the X-ray experiments lateral scanning along the surface is performed to distribute the X-ray dose.[35,38]

For temperature-dependent studies, the wafers were annealed using a heating stage (DHS 1100, Anton Paar GmbH, Austria), prior to the GISAXS measurements. Prior to each measurement a waiting time of 5 min was employed to reach a temperature equilibrium.

Field-Emission Scanning Electron Microscopy: FE-SEM analysis was performed on a Hitachi S-4800 to investigate the pristine thin films as well as after annealing at 40 °C. The acceleration voltage was kept at 1.0 and 3.0 kV if nothing else was stated and pictures were acquired at different magnifications, stated in each image. The samples were mounted on a metal stub with carbon tape and coated with a 5 nm layer of Pt/Pd with a Cressington 208HR sputter coater.

Atomic Force Microscopy: All samples were analyzed using a Multimode 8 (Bruker, USA) AFM in the tapping ScanAsyst-Air mode, using a silicon nitride-based cantilever with 130 kHz resonance frequency, a nominal spring constant of 0.4 Nm^{-1}, and a tip radius of 2 nm (ScanAsyst-AIR-HR, Bruker, USA).

Contact Angle Measurements: CAM were performed on the coated silicon substrates either pristine or heat treated in an oven (normal atmosphere) for 1 h at 40 °C or 140 °C. Wafers were kept in a humidity controlled room at 50%RH and 23 °C for 24 h followed by analysis at the same conditions using a KSV instrument (CAM 200) equipped with a Basler A602f camera, using 3 µL droplets of MilliQ-water. A Young-Laplace fitting mode supplied by KSV was used to process the images. The CA values reported were those observed after 20 s of measurement when the drop had reached its equilibrium after spreading on the substrates.

Supporting Information

Supporting Information is available from the Wiley Online Library or from the author.

Conflict of Interest

The authors declare no conflict of interest.

[1] M. Rao, G. Samarnayake, J. Marlow, R. Tomko, in *ACS Symposium Series*, Vol. *1178*, American Chemical Society, Washington, DC, USA **2014**, p. 193.

[2] J. L. Keddie, *Mater. Sci. Eng.: R: Rep.* **1997**, *21*, 101.

[3] J. Zhou, J. Wang, Y. Huang, G. Liu, L. Wang, S. Chen, X. Li, D. Wang, Y. Song, L. Jiang, *NPG Asia Mater.* **2012**, *4*, e21.

[4] Q. Chen, S. C. Bae, S. Granick, *Nature* **2011**, *469*, 381.

[5] J.-K. Pi, J. Yang, Q. Zhong, M.-B. Wu, H.-C. Yang, M. Schwartzkopf, S. V. Roth, P. Müller-Buschbaum, Z.-K. Xu, *ACS Appl. Nano Mater.* **2019**, *2*, 4556.

[6] B. Li, D. Zhou, Y. Han, *Nat. Rev. Mater.* **2016**, *1*, 15011.

[7] T. P. Bigioni, X.-M. Lin, T. T. Nguyen, E. I. Corwin, T. A. Witten, H. M. Jaeger, *Nat. Mater.* **2006**, *5*, 265.

[8] D. Ryan, L. Nagle, D. Fitzmaurice, *Nano Lett.* **2004**, *4*, 573.

[9] P. A. Steward, J. Hearn, M. C. Wilkinson, *Adv. Colloid Interface Sci.* **2000**, *86*, 195.

[10] R. D. Deegan, O. Bakajin, T. F. Dupont, G. Huber, S. R. Nagel, T. A. Witten, *Nature* **1997**, *389*, 827.

[11] E. Aramendia, J. Mallégol, C. Jeynes, M. J. Barandiaran, J. L. Keddie, J. M. Asua, *Langmuir* **2003**, *19*, 3212.

[12] H. A. S. Schoonbrood, J. M. Asua, *Macromolecules* **1997**, *30*, 6034.

[13] P. J. Feeney, D. H. Napper, R. G. Gilbert, *Macromolecules* **1987**, *20*, 2922.

[14] A. Darabi, A. R. Shirin-Abadi, J. Pinaud, P. G. Jessop, M. F. Cunningham, *Polym. Chem.* **2014**, *5*, 6163.

[15] M. Lansalot, J. Rieger, F. D'Agosto, in *Macromolecular Self-Assembly*, John Wiley & Sons, Inc., Hoboken, New Jersey, **2016**; p. 33.

[16] W. J. Priest, *J. Phys. Chem.* **1952**, *56*, 1077.

[17] J. M. Asua, *J. Polym. Sci., Part A: Polym. Chem.* **2004**, *42*, 1025.

[18] C. D. Anderson, E. S. Daniels, *Emulsion Polymerisation and Latex Applications*, Vol. *14*, Rapra Technology Limited, Shawbury, UK **2003**.

[19] L. Isa, F. Lucas, R. Wepf, E. Reimhult, *Nat. Commun.* **2011**, *2*, 438.

[20] M. E. Roberts, S. C. B. Mannsfeld, R. M. Stoltenberg, Z. Bao, *Org. Electron.* **2009**, *10*, 377.

[21] K. L. Menzies, L. Jones, *Optom. Vis. Sci.* **2010**, *87*, 387.

[22] E. E. Brotherton, F. L. Hatton, A. A. Cockram, M. J. Derry, A. Czajka, E. J. Cornel, P. D. Topham, O. O. Mykhaylyk, S. P. Armes, *J. Am. Chem. Soc.* **2019**, *141*, 13664.

[23] A. M. dos Santos, J. Pohn, M. Lansalot, F. D'Agosto, *Macromol. Rapid Commun.* **2007**, *28*, 1325.

[24] T. Boursier, I. Chaduc, J. Rieger, F. D'Agosto, *Polym. Chem.* **2011**, *2*, 355.

[25] I. Chaduc, W. Zhang, J. Rieger, M. Lansalot, F. D'Agosto, B. Charleux, *Macromol. Rapid Commun.* **2011**, *32*, 1270.

[26] J. Engström, F. L. Hatton, L. Wågberg, F. D'Agosto, M. Lansalot, E. Malmström, A. Carlmark, *Polym. Chem.* **2017**, *8*, 1061.

[27] L. Carlsson, A. Fall, I. Chaduc, L. Wågberg, B. Charleux, E. Malmström, F. D'Agosto, M. Lansalot, A. Carlmark, *Polym. Chem.* **2014**, *5*, 6076.

[28] J. Engström, T. Benselfelt, L. Wågberg, F. D'Agosto, M. Lansalot, A. Carlmark, E. Malmström, *Nanoscale* **2019**, *11*, 4287.

[29] D. Grosso, F. Cagnol, G. J. deA. A. Soler-Illia, E. L. Crepaldi, H. Amenitsch, A. Brunet-Bruneau, A. Bourgeois, C. Sanchez, *Adv. Funct. Mater.* **2004**, *14*, 309.

[30] J. Huang, R. Fan, S. Connor, P. Yang, *Angew. Chem., Int. Ed.* **2007**, *46*, 2414.

[31] Y. Lu, R. Ganguli, C. A. Drewien, M. T. Anderson, C. J. Brinker, W. Gong, Y. Guo, H. Soyez, B. Dunn, M. H. Huang, J. I. Zink, *Nature* **1997**, *389*, 364.

[32] P. Colson, R. Cloots, C. Henrist, *Langmuir* **2011**, *27*, 12800.

[33] H. Jiang, K. Yu, Y. Wang, *Opt. Lett.* **2007**, *32*, 575.

[34] R. Gupta, K. D. M. Rao, K. Srivastava, A. Kumar, S. Kiruthika, G. U. Kulkarni, *ACS Appl. Mater. Interfaces* **2014**, *6*, 13688.

[35] C. J. Brett, N. Mittal, W. Ohm, M. Gensch, L. P. Kreuzer, V. Körstgens, M. Månsson, H. Frielinghaus, P. Müller-Buschbaum, L. D. Söderberg, S. V. Roth, *Macromolecules* **2019**, *52*, 4721.

[36] R. Blell, X. Lin, T. Lindström, M. Ankerfors, M. Pauly, O. Felix, G. Decher, *ACS Nano* **2017**, *11*, 84.

[37] J. J. Richardson, M. Bjornmalm, F. Caruso, *Science.* **2015**, *348*, aaa2491.

[38] S. V Roth, *J. Phys.: Condens. Matter* **2016**, *28*, 403003.

[39] W. Ohm, A. Rothkirch, P. Pandit, V. Körstgens, P. Müller-Buschbaum, R. Rojas, S. Yu, C. J. Brett, D. L. Söderberg, S. V Roth, *J. Coat. Technol. Res.* **2018**, *15*, 759.

**ADVANCED
SCIENCE NEWS**

www.advancedsciencenews.com

**ADVANCED
FUNCTIONAL
MATERIALS**

www.afm-journal.de

[40] P. Zhang, G. Santoro, S. Yu, S. K. Vayalil, S. Bommel, S. V. Roth, *Langmuir* **2016**, *32*, 4251.

[41] M. Al-Hussein, M. Schindler, M. A. Ruderer, J. Perlich, M. Schwartzkopf, G. Herzog, B. Heidmann, A. Buffet, S. V. Roth, P. Müller-Buschbaum, *Langmuir* **2013**, *29*, 2490.

[42] Y. Zhang, D. Ge, S. Yang, *J. Colloid Interface Sci.* **2014**, *423*, 101.

[43] R. R. Prabhakar, N. Huu Loc, M. H. Kumar, P. P. Boix, S. Juan, R. A. John, S. K. Batabyal, L. H. Wong, *ACS Appl. Mater. Interfaces* **2014**, *6*, 17661.

[44] K. C. Krogman, N. S. Zacharia, S. Schroeder, P. T. Hammond, *Langmuir* **2007**, *23*, 3137.

[45] L. La Notte, L. Salamandra, A. Zampetti, F. Brunetti, T. M. Brown, A. Di Carlo, A. Reale, *Int. J. Photoenergy* **2012**, *2012*, 1.

[46] G. Herzog, G. Benecke, A. Buffet, B. Heidmann, J. Perlich, J. F. H. Risch, G. Santoro, M. Schwartzkopf, S. Yu, W. Wurth, S. V. Roth, *Langmuir* **2013**, *29*, 11260.

[47] Y. Lin, A. Böker, J. He, K. Sill, H. Xiang, C. Abetz, X. Li, J. Wang, T. Emrick, S. Long, Q. Wang, A. Balazs, T. P. Russell, *Nature* **2005**, *434*, 55.

[48] S. Hu, J. Rieger, Y. Lai, S. V Roth, R. Gehrke, Y. Men, *Macromolecules* **2008**, *41*, 5073.

[49] J. Richard, K. Wong, *J. Polym. Sci., Part B: Polym. Phys.* **1995**, *33*, 1395.

[50] L. Wu, X. Wang, G. Wang, G. Chen, *Nat. Commun.* **2018**, *9*, 1335.

[51] A. Hexemer, P. Müller-Buschbaum, *IUCrJ* **2015**, *2*, 106.

[52] G. Herzog, M. M. Abul Kashem, G. Benecke, A. Buffet, R. Gehrke, J. Perlich, M. Schwartzkopf, V. Körstgens, R. Meier, M. A. Niedermeier, M. Rawolle, M. A. Ruderer, P. Müller-Buschbaum, W. Wurth, S. V. Roth, *Langmuir* **2012**, *28*, 8230.

[53] W. A. Lopes, H. M. Jaeger, *Nature* **2001**, *414*, 735.

[54] W. Liu, J. Midya, M. Kappl, H.-J. Butt, A. Nikoubashman, *ACS Nano* **2019**, *13*, 4972.

[55] C.-A. Fustin, G. Glasser, H. W. Spiess, U. Jonas, *Adv. Mater.* **2003**, *15*, 1025.

[56] F. Lin, D. J. Meier, *Langmuir* **1995**, *11*, 2726.

[57] A. F. Routh, W. B. Russel, *Langmuir* **1999**, *15*, 7762.

[58] E. Pérez, J. Lang, *Macromolecules* **1999**, *32*, 1626.

[59] J. L. Keddie, R. A. L. Jones, R. A. Cory, *Faraday Discuss.* **1994**, *98*, 219.

[60] Y. Grohens, M. Brogly, C. Labbe, M.-O. David, J. Schultz, *Langmuir* **1998**, *14*, 2929.

[61] C. J. Schaffer, C. M. Palumbiny, M. A. Niedermeier, C. Jendrzejewski, G. Santoro, S. V. Roth, P. Müller-Buschbaum, *Adv. Mater.* **2013**, *25*, 6760.

[62] B. Su, H. A. Caller-Guzman, V. Körstgens, Y. Rui, Y. Yao, N. Saxena, G. Santoro, S. V. Roth, P. Müller-Buschbaum, *ACS Appl. Mater. Interfaces* **2017**, *9*, 43724.

[63] Y. Ma, X. Cao, X. Feng, Y. Ma, H. Zou, *Polymer.* **2007**, *48*, 7455.

[64] Z. Li, W. Meng, J. Tong, C. Zhao, F. Qin, F. Jiang, S. Xiong, S. Zeng, L. Xu, B. Hu, Y. Zhou, *Sol. Energy Mater. Sol. Cells* **2015**, *137*, 311.

[65] M.-R. Ahmadian-Yazdi, A. Rahimzadeh, Z. Chouqi, Y. Miao, M. Eslamian, *AIP Adv.* **2018**, *8*, 025109.

[66] G. Bouhadir, N. Legrand, B. Quiclet-Sire, S. Z. Zard, *Tetrahedron Lett.* **1999**, *40*, 277.

[67] S. H. Thang, (B) Y. K. Chong, R. T. A. Mayadunne, G. Moad, E. Rizzardo, *Tetrahedron Lett.* **1999**, *40*, 2435.

[68] D. Horn, in *Progress in Colloid and Polymer Science*, Vol. *264*, Steinkopff, Darmstadt **1978**, p. 251.

[69] P. Jenny, D. Roekaerts, N. Beishuizen, *Prog. Energy Combust. Sci.* **2012**, *38*, 846.

[70] A. Buffet, A. Rothkirch, R. Döhrmann, V. Körstgens, M. M. Abul Kashem, J. Perlich, G. Herzog, M. Schwartzkopf, R. Gehrke, P. Müller-Buschbaum, S. V. Roth, *J. Synchrotron Radiat.* **2012**, *19*, 647.

1907720 (9 of 9)